MNRAS 000, 1–14 (2017) Preprint 16 February 2017 Compiled using MNRAS LATEX style file v3.0

Relativistic simulations of long-lived reverse shocks in stratified ejecta: the origin of flares in GRB afterglows

A. Lamberts[1⋆] and F. Daigne[2]
[1] *Theoretical Astrophysics, California Institute of Technology, Pasadena, CA 91125, USA*
[2] *UPMC-CNRS, UMR7095, Institut d'Astrophysique de Paris, F-75014 Paris, France*

arXiv:1702.04362v1 [astro-ph.HE] 14 Feb 2017

16 February 2017

ABSTRACT

The X-ray light curves of the early afterglow phase from gamma-ray bursts present a puzzling diversity, including flares. The origin of these flares is still debated, and often associated with a late activity of the central engine. We discuss an alternative scenario where the central engine remains short-lived and flares are produced by the propagation of a long-lived reverse shock in a stratified ejecta. We use a set of one-dimensional ultrarelativistic hydrodynamic simulations with different initial internal structure in the gamma-ray burst ejecta. We use them to extract bolometric light curves and compare them with a previous study based on a simplified ballistic model. We find a good agreement between the two approaches, with similar slopes and variability in the light curves, but identify several weaknesses in the ballistic model: the density is underestimated in the shocked regions, and more importantly, late shock reflections are not captured. With the accurate dynamics provided by our hydrodynamic simulations, we confirm that internal shocks in the ejecta lead to the formation of dense shells. The interaction of a long-lived reverse shock with these dense shells then produces bright flares in the bolometric light curve, with arrival times, shapes, and duration in agreement with the observed properties of X-ray flares in GRB afterglows.

Key words: hydrodynamics, relativistic processes, shock waves, methods:numerical, gamma-ray burst:general, radiation mechanisms: non-thermal

1 INTRODUCTION

Gamma-ray bursts (GRB) are intense flashes of gamma-rays of extragalactic origin, with an apparent rate of about once a day. Their duration shows a bimodal distribution, with long bursts (from a few seconds to a few minutes) associated with the collapse of some massive stars (Woosley 1993; Medvedev & Loeb 1999), and short bursts (from a few milliseconds to a few seconds) believed to originate from mergers of compact objects in a binary system (see Berger 2014, for a review). The prompt emission peaks in the keV-MeV range and is followed by a rapidly fading afterglow observed on longer timescales from the X-ray to the radio wavelengths (see Zhang et al. 2016, for a recent review).

The initial event leads to the formation of a new compact source, probably an accreting black hole, even if rapidly rotating magnetars are also discussed (Troja et al. 2007; Rowlinson et al. 2013). The highly variable prompt emission corresponds to a tremendous energy radiated in gamma-rays ($E_{\rm iso} \sim 10^{51} - 10^{54}$ erg) and must be emitted through internal dissipation within a highly relativistic outflow to avoid a strong $\gamma\gamma$ annihilation. The afterglow is due to the deceleration of the relativistic outflow by the external medium. In the standard scenario, the afterglow emission is due to the synchrotron radiation of non-thermal electrons accelerated at the ultra-relativistic (external) forward shock (see Kumar & Zhang 2015, for a recent review). This naturally leads to an observed flux $F_\nu \propto t_{\rm obs}^{-\alpha}$ with $\alpha \simeq 1$ (Mészáros & Rees 1997; Sari et al. 1998), in agreement with observations a few hours after the burst.

However, this simple picture was soon challenged by the first observations with the *Swift* satellite (Gehrels et al. 2004), which revealed a great diversity of light curves, especially in the early afterglow phase, and an unexpected variability in the X-ray afterglow. The latter can show an early steep decay just after the prompt emission ($\alpha \simeq 3$), often followed by a plateau phase ($\alpha \simeq 0$) before the standard decay ($\alpha \simeq 1$) (Tagliaferri et al. 2005; Nousek et al. 2006; O'Brien et al. 2006). In addition, X-ray flares are observed in $\sim 30\%$ of GRBs (see e.g Burrows et al. 2005a; Chincarini et al. 2010), with some bursts presenting several flares between a few 10 s and several 10^4 s after the trigger. The underlying shape of the X-ray light curve remains unaffected by the flares. The flares are asymmetric, with a steep rise and a slower decay (Chincarini et al. 2007). However, contrary to the gamma-ray variability observed during the prompt phase, the X-ray flares present a common behavior with duration increasing with time, following $\Delta t_{\rm obs}/t_{\rm obs} \simeq 0.1 - 0.3$.

This observed diversity and variability of the X-ray afterglow

⋆ E-mail:lamberts@caltech.edu

© 2017 The Authors

is difficult to reconcile with the standard external shock model. In particular, the emission is only mildly sensitive to the structure of the external medium (e.g. Dai & Lu 2002; Ramirez-Ruiz et al. 2005; Margutti et al. 2011; Gat et al. 2013). Plateaus can be reproduced with late energy injection (Rees & Mészáros 1998) and flares can be associated with late internal dissipation in the ejecta in the case of a long-lasting central engine (e.g. Burrows et al. 2005b; Zhang et al. 2006; Fan & Wei 2005; Margutti et al. 2011). Such possibilities put strong constraints on the energetics and lifetime of the source. Few alternatives without such constraints have been proposed (see e.g. the photospheric emission from slow material ejected together with the GRB relativistic ejecta recently proposed by Beniamini & Kumar 2016).

On the other hand, the emission of the reverse shock propagating within the ejecta is very sensitive to the structure of the ejecta and may provide an alternative explanation. Sari & Mészáros (2000) showed that this reverse shock emission can be long-lasting, if the ejecta ends with a tail of low Lorentz factor material. Uhm & Beloborodov (2007); Genet et al. (2007) proposed that such a long-lived reverse shock (LLRS) may dominate the observed emission and could easily produce plateaus. The capacity of this model to reproduce the diversity of the observed X-ray and optical light curves, including plateaus and chromatic breaks was successfully tested by Hascoët et al. (2011, 2012); Uhm et al. (2012). Several observed correlations between the prompt and plateau properties can also be accounted for (Hascoët et al. 2014).

Hascoet et al. (2015) suggested that this scenario could also naturally explain flares, alleviating the constraints on the lifetime and variability of the central engine. The flares are associated with the propagation of the LLRS through dense shells within the ejecta, which are expected to appear after the development of internal shocks. Hascoet et al. (2015) presented simplified simulations based on a ballistic model (Daigne & Mochkovitch 1998) and computed bolometric light curves assuming an anisotropic emission in the comoving frame (Beloborodov et al. 2011). They obtained asymmetric flares with $\Delta t_{\rm obs}/t_{\rm obs} \simeq 0.1 - 0.3$. In the present paper, we validate this promising scenario by performing relativistic hydrodynamical simulations to compute the dynamics of the interaction of the LLRS with a structured ejecta.

Fully modeling the propagation of a LLRS is a numerical challenge. On one hand, one needs a high enough resolution to properly model the internal shocks. On the other hand, one needs to follow the ejecta beyond the deceleration radius to follow the impact of the LLRS. As such, multidimensional simulations have specifically focused on the internal shock phase (see e.g. Aloy et al. 2000; Duffell & MacFadyen 2015) or the deceleration phase (Meliani et al. 2007; Mimica et al. 2009; van Eerten et al. 2010; De Colle et al. 2012). Currently, parameter exploration including both phases can only be achieved with 1D simulations. In this paper, we perform 1D relativistic hydrodynamic simulations to assert the validity and limits of the ballistic model described in Hascoet et al. (2015). In §2 we describe our numerical methods and the setup of our set of simulations. In §3 we analyze the hydrodynamic structure of the ejecta and compute the resulting bolometric flux and compare to the ballistic model in §4. We discuss the observability of flares in §5 and conclude (§6).

2 NUMERICAL METHODS

2.1 Relativistic RAMSES

Our numerical method is based on the relativistic extension of the RAMSES code (Teyssier 2002), presented in Lamberts et al. (2013). The code computes the evolution of the conserved variables in the frame of the laboratory

$$\mathbf{U} = \begin{pmatrix} D \\ M \\ E \end{pmatrix} = \begin{pmatrix} \Gamma\rho \\ \Gamma^2\rho v\frac{h}{c^2} \\ \Gamma^2\rho h - P \end{pmatrix}, \tag{1}$$

where D is the density, M the momentum density and E the energy density. h is the specific enthalpy, ρ is the proper mass density, v is the fluid velocity, P is the gas pressure. The Lorentz factor is given by $\Gamma = (1 - v^2/c^2)^{-1/2}$. Within the relativistic hydrodynamics (RHD) simulation, the equations are solved with all velocities normalized to the speed of light. We neglect the dynamical impact of magnetic fields. While the numerical scheme in our simulation and in Lamberts et al. (2013) are strictly identical, we use a one-dimensional spherical grid and do not include adaptive mesh refinement in the simulations presented here.

In one-dimensional spherical coordinates, the RHD equations along the radial axis are given by

$$\begin{aligned} \frac{\partial D}{\partial t} + \frac{\partial Dv}{\partial r} &= -\frac{2}{r}Dv \\ \frac{\partial M}{\partial t} + \frac{\partial (Mv + P)}{\partial r} &= -\frac{2}{r}Mv \\ \frac{\partial E}{\partial t} + \frac{\partial Mc^2}{\partial r} &= -\frac{2}{r}Mc^2. \end{aligned} \tag{2}$$

The right hand side of the equations corresponds to the so-called source terms related to the spherical coordinates. A passive scalar s is included in the simulations using $S = s\rho\Gamma$ in the laboratory frame and $F = \rho s v \Gamma$ to compute its flux. As explained below, this allows to distinguish the GRB ejecta from the external medium, or different regions in the ejecta. Eqs. 2 are closed with the following equation of state

$$P = (\gamma - 1)(e - \rho) \tag{3}$$

where e is the sum of the internal energy and the rest mass energy of the fluid. We assume an ultrarelativistic fluid with $\gamma = 4/3$. We use the HLLC Riemann solver and a Minmod slope limiter. Due to the spherical expansion of the ejecta, the density and pressure in the inner part of the ejecta become very small and hard to handle numerically. Therefore, we floor the density and pressure to 10^{-10}.

2.2 Moving grid

As the width of the ejecta of the GRB Δ is small compared to the deceleration radius $R_{\rm dec}$, a static grid is not well fit. Instead, we have implemented a moving grid that follows the motion of the ejecta. The grid has a fixed physical width $L_{\rm box}$, which is large enough to cover most of the ejecta at the observer time $t_{\rm obs}$ we are interested in. At each timestep, we compute the position of the forward shock, defined by the outermost cell where the density is at least a thousand times higher than in the next cell. When the forward shock has reached $R_{\rm edge}$, we shift the grid towards higher radii. The innermost $n_{\rm shift}$ cells are suppressed, the contents of all other cells are shifted towards the left and $n_{\rm shift}$ new cells are created on the right side of the simulation. These cells are filled with

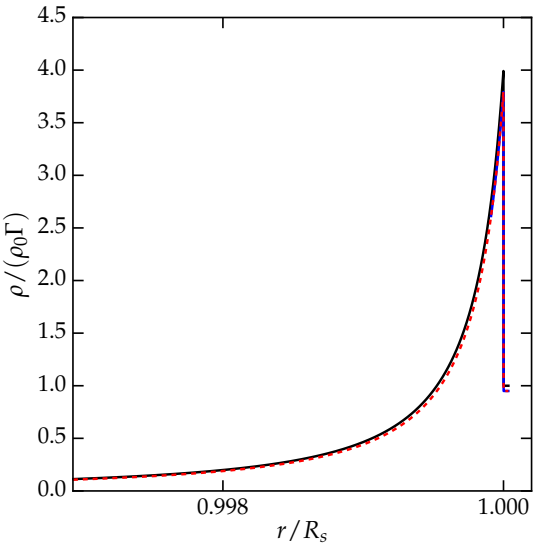

Figure 1. Validation of the numerical method based on the normalized density in a 1D spherical blast wave. The simulation on a standard grid (dashed red line), on a moving grid (solid blue line) and the analytic Blandford-McKee solution (solid black line) are in very good agreement, when the forward shock, located at R_s reaches the deceleration radius $R_{\rm dec}$. The initial energy of the ejecta is 10^{53} erg and it propagates in an external medium with $n_0 = 10^3$ cm^{-3}.

the user-defined external medium. In our simulations we arbitrarily set $R_{\rm edge} = n_{\rm shift} = 100$. We checked that the exact value of $R_{\rm edge}$ and $n_{\rm shift}$ does not impact the outcome of the simulation.

Fig. 1 shows the evolution of a relativistic blast wave as it propagates and expands. The simulation with the moving grid shows the same results as the simulation on the complete grid and is very close to the analytic Blandford-McKee solution (Blandford & McKee 1976). Both simulations have the same equivalent resolution and the moving grid simulation takes roughly ten times less to complete, while modeling most of the mass of the ejecta. While this method perfectly tracks the ejecta over long distances, care has to be taken at the inner boundary. As such, in this specific simulation we set the boundary condition to match the analytic solution.

2.3 Setup of the simulations

We perform a set of simulations, modeling different levels of complexity in the initial ejecta by varying the initial distribution of the Lorentz factor $\Gamma(r)$ as discribed below. The density is then given by

$$\rho(r) = \frac{\dot{E}}{4\pi r^2 v(r)\Gamma^2(r)c^2\left(1+\eta\left(\frac{\gamma}{\gamma-1}-\frac{1}{\Gamma(r)^2}\right)\right)}, \quad (4)$$

where $\dot{E}$ is the power injected in the ejecta and $\eta = 10^{-3}$ the ratio between pressure P and the rest mass energy density. The initial width of the ejecta is set by the duration of the burst $\Delta = ct_{\rm w}$. In all our simulations we have $t_{\rm w} = 100$ s, $\dot{E} = 10^{51}$ erg s^{-1}.

The initial inner (R_Δ) and outer radii (R_0) of the ejecta are set to $R_\Delta/c = 100$ s ($\simeq 3\times10^{12}$ cm) and $R_0/c = 200$ s ($\simeq 6\times10^{12}$ cm). As such, our simulation starts at $t = 200$ s after the start of the relativistic ejection. In all the following, the origin of time is the actual ejection, meaning that our first snapshot is slightly after 200 s. As such, we do not model the initial acceleration of the ejecta.

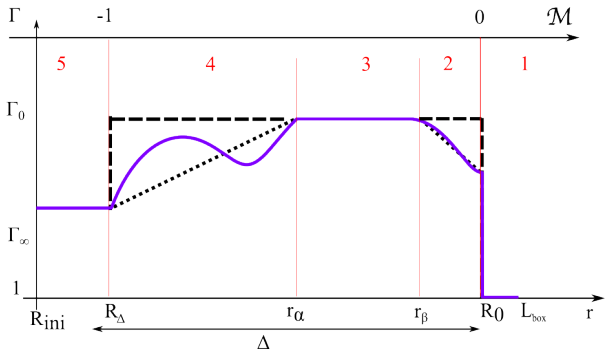

Figure 2. Initial distribution of the Lorentz factor in the simulations. The ejecta extends from R_Δ to R_0 and the computational box from $R_{\rm ini}$ to $L_{\rm box}$. In the simplest case, the ejecta is uniform (dashed line), while in more complex simulations it includes a tail and/or head region. These outer regions can present a linear variation of the Lorentz factor (dotted line) or present a sinusoidal variation (blue solid line) which will lead to internal shocks. The vertical red lines show the initial separation of each region in the simulations, with the corresponding values of the passive scalar given in red. The Lagrangian coordinates are indicated on the upper axis.

Fig. 2 provides a schematic view of different initial setups of the Lorentz factor. In the most general case the ejecta displays variability in both the head and tail region (blue solid line) and we have

$$\begin{aligned}
\Gamma_5(r) &= \Gamma_\infty \\
\Gamma_4(r) &= \left(\Gamma_0 - (\Gamma_\infty-\Gamma_0)\frac{r-R_\Delta}{\alpha}\right)\left[1+A\sin\left(2\pi\frac{r-R_\Delta}{\alpha}\right)\right] \\
\Gamma_3(r) &= \Gamma_0 \\
\Gamma_2(r) &= \Gamma_0\left[\frac{1+k}{2}+\frac{1-k}{2}\cos\left(\pi\frac{r-r_\beta}{R_0-r_\beta}\right)\right] \\
\Gamma_1(r) &= 1.
\end{aligned} \quad (5)$$

with

$$r_\alpha = R_0 + (\alpha-1)\Delta \quad (6)$$

$$r_\beta = R_0 + (\beta-1)\Delta. \quad (7)$$

Table 1 lists the values of A, k, α and β in our simulations. We always adopt $\Gamma_0 = 100$ and $\Gamma_\infty = 10$. If the central engine switches off smoothly, one could expect $\Gamma_\infty \simeq 1$. However, this would give a very long deceleration time and radius which are very hard to model numerically. As we are mostly interested in the X-ray variability in the early afterglow phase, our high value is a reasonable approximation. The passive scalar tracks the evolution of different initial regions of the ejecta. The values are indicated on the top row of Fig. 2. The external density is set to $n_0 = 1000$ cm $^{-3}$ except for *run5b*, which is identical to *run5* but has $n_0 = 32$ cm^{-3}.

The initial outer edge of the box is located at $L_{\rm box}/c = 600$ s and we use $N = 96000$ grid cells. This gives a final resolution of $\Delta r = 1.7\times10^8$ cm, equivalent to a temporal resolution of about 5 milliseconds. Tests with $N = 48000$ and $N = 192000$ grid cells for *run4* show that the structure of the forward shock is identical in all cases but the internal shocked regions are denser and narrower at higher resolution. However, the Lorentz factor is the same in the whole box for all tests. When comparing the final light curves, we find no difference for the luminosity of the forward shock beyond $t_{\rm obs} = 10$ s. We find that the total luminosity of the other shocks is higher at higher resolution, with a time-independent offset of about

Table 1. Parameters for the simulations.

name	A	k	α	β	n_0 (cm^{-3})	description
run1	0	1	0	1	10^3	uniform
run2	0	1	0.5	1	10^3	tail
run3	0	0.25	0.5	0.2	10^3	tail+head
run4	0.6	1	0.5	1	10^3	variable tail
run5	0.6	0.25	0.5	0.2	10^3	variable tail+head
run5b	0.6	0.25	0.5	0.2	32	variable tail+head

13 per cent between the $N = 48000$ and $N = 96000$ runs and a 5 per cent offset between the $N = 96000$ and $N = 192000$ runs. In all cases, the slopes and variations in the light curves are very similar, indicating that our simulations have enough resolution to study the impact of a LLRS on the light curves. The parameters we choose are a compromise between the extreme nature of the ejecta and numerical constraints.

We stop the simulation at the end of the early afterglow phase, about 2×10^6 s after the initial ejection. At that stage, most of the internal structure of the ejecta has been washed out by shocks and the later evolution would tend to the Blandford-McKee solution (Blandford & McKee 1976) and then a Sedov solution in the non-relativistic limit (Sedov 1969).

2.4 Shock detection algorithm

To derive light curves from the hydrodynamic structure of the ejecta, we need to determine the energy dissipated in all shocked regions. Common methods to detect shocks include finding important jumps in density and/or pressure or searching for compressed regions ($\nabla \cdot v < 0$) (Corrales et al. 2010). Such methods are only successful for very strong shocks, and fail to detect internal shocks in the ejecta. Therefore, we use a relativistic shock finding algorithm, inspired by Zanotti et al. (2010). The algorithm is based on the predictions of the wave patterns of the relativistic Riemann problem (Rezzolla et al. 2003; Rezzolla & Zanotti 2002). A shock occurs when the velocity gradient Δv between two adjacent cells is greater than a certain threshold $\tilde{v}$, determined by the thermodynamics of the fluid. In practice, for both directions of propagation, we compute the local minima of $V = \tilde{v} - \Delta v$ to determine the locations of the shocks. To avoid spurious detections of very weak shocks, we smooth V over 10 computational cells. This step was not present in Zanotti et al. (2010), who instead suggested to include a small correction to V to avoid spurious detections.

The determination of the up- and downstream properties of the flow is less precise, as the shocks are smeared out due to numerical diffusion and may interact with each other and the contact discontinuity between the ejecta and the shocked external medium. The spreading of the shocks is most notable at very early times, when shocks are still forming. For a forward/backward propagating shock, we find the cell of maximal density (corrected for the spherical geometry) in the region between 150 and 100 cells before/after the shock location. The downstream density, pressure and Lorentz factor are set to the values in that cell. For the upstream variables, we consider the mean over the cells between 100 and 150 after/before the shock. Visual inspection of the shock locations and conditions confirms the accuracy of the method for $t > 10^5$ s. At earlier times visual determination of the up-and-downstream regions is somewhat arbitrary. However, the hydrodynamic variables we recover respect the Rankine-Hugoniot jump conditions within 10 per cent after $t = 10^4$ s. We tested alternate methods to find the downstream variables at earlier times and found no impact on the light curves beyond $t_{obs} = 10$ s. As such, we are confident that our method yields reliable values for the up- and downstream regions and luminosity at the timescales relevant to our study.

The detection of the contact discontinuity between the ejecta and the external medium is made possible with the passive scalar, which values are shown on Fig. 2. For the runs without head region (*run1, run2, run4*) we set the position of the contact discontinuity r_{CD} to be the cell where the passive scalar is the closest to 2. For the runs with head region (*run3, run5*), we set r_{CD} to the cell where the passive scalar is closest to 1.5.

2.5 Limits of 1D RHD simulations

The RHD simulations and ballistic model we present are one-dimensional, which enables us to cover a wide range of parameters and study the evolution of the ejecta from the internal shock phase until the deceleration phase. In the ultrarelativistic ejecta we are considering ($\Gamma \geqslant 10$ at the end of the simulation), the lateral expansion of the jet can be safely neglected and our 1D simulations provide a good model of the global dynamics. Multidimensional simulations show the development of hydrodynamic instabilities (Aloy et al. 1999; Duffell & MacFadyen 2013) at the contact discontinuity between the outside medium and the ejecta. While the latter lead to important mixing, they do not strongly affect the structure of the internal and reverse shocks. Duffell & MacFadyen (2013) show that reverse shocked is pushed away from the forward shock and its emission is more delayed. We do not expect this to qualitatively impact the results presented here.

Our models also neglect the dynamical impact of the magnetic fields. While the traditional fireball model relies on thermal pressure to accelerate the ejecta, magnetic fields are also promising candidates for the acceleration and collimation of the ejecta during the early phases (see Granot et al. 2015, for a review of magnetic field in GRB). At later stages, Mimica et al. (2009) show that when the magnetization is of order unity or above, the propagation of shocks is suppressed and one has to invoke magnetic reconnection to explain the observed emission (Narayan et al. 2011). As the scenario studied in this paper relies on a complex dynamical evolution related to several generations of shocks, we clearly assume that the ejecta at large distance of the source has a low magnetization ($\sigma \leqslant 0.1$).

2.6 Ballistic model

If the magnetization is small, the GRB ejecta at large distance from the source is dominated by its kinetic energy. It is then possible to model it using a ballistic approach where pressure waves are neglected. This method is described by Daigne & Mochkovitch (1998) for the internal shock phase: the outflow is discretized in a large number of shells which interact only by direct collisions. A sequence of collisions models the propagation of a shock wave. The comparison with a fully relativistic hydrodynamic simulation shows that the ballistic model recovers most features of the evolution (Daigne & Mochkovitch 2000), except for the density in the shocked regions, which is usually underestimated.

This approach has been extended by Genet et al. (2007); Hascoët et al. (2011, 2012, 2014) to include the deceleration phase. This allows to follow the forward shock in the external medium and the reverse shock in the ejecta. The limitations are the same:

the radius and Lorentz factor of the different shocks are correctly estimated, as well as the dissipated power, but the density is underestimated. The advantage of the ballistic approach is its very low computational cost, which allows to explore a large domain of parameters for the model. The scenario where afterglow flares are produced by the interaction of a LLRS with dense shells in the ejecta has been explored using the ballistic approach by Hascoet et al. (2015). The promising results motivated the present study. In the following, we compare our results obtained with the fully relativistic hydrodynamic code described above with the same ejecta modeled with the ballistic approach and identify the different features that will contribute to the light curves.

3 HYDRODYNAMICS OF THE EJECTA

3.1 Uniform ejecta

Fig. 3 shows the density and Lorentz factor in *run1*,which we consider as our reference model. The initial state (purple line) corresponds to a uniform shell of width $ct_{\rm w} = 3.0 \times 10^{12}$ cm with a Lorentz factor $\Gamma_0 = 100$, an energy $E_0 = 10^{53}$ erg and a mass $M_0 = \frac{E_0}{\Gamma_0 c^2} = 1.1\,10^{32}$ g. After describing the evolution in this simple case, we will progressively describe and explain the impact of various features in the setup on the dynamical evolution of the ejecta. We use a Lagrangian description to facilitate identification of different discontinuities. The x-axis shows the accumulated mass fraction normalized by the initial mass of the ejecta:

$$\mathcal{M}(R) = \frac{1}{M_0}\int_{r_{CD}}^{R} 4\pi r^2\,\rho\Gamma dr\,. \qquad (8)$$

As such, we use negative values for the ejecta and positive values for the shocked external medium.

With our initial conditions, the spreading radius of the ejecta is of the order of $R_{\rm spread} \simeq \Gamma_0^2\Delta \simeq 3.0\times10^{14}$ cm and the deceleration radius $R_{\rm dec} \simeq \left(\frac{3}{4\pi}\frac{\dot{E}t_{\rm w}}{\Gamma_0^2 n_0 m_{\rm p}c^2}\right)^{1/3} \simeq 1.2\times10^{16}$ cm. The condition $R_{\rm spread} \ll R_{\rm dec}$ corresponds to the case where the reverse shock is initially non-relativistic, becomes progressively relativistic, and crosses the ejecta at $R_{\rm cross} \simeq R_{\rm spread}^{1/4}R_{\rm dec}^{3/4} \simeq 4.8\,10^{15}$ cm $\simeq 0.4R_{\rm dec}$, before the deceleration radius (Sari & Piran 1995; Kobayashi et al. 1999). This is indeed observed in our simulation. After $t = 2\times10^5$ s, i.e. $R \simeq 0.5\,R_{\rm dec}$ (blue line), the forward shock is still very close to the contact discontinuity and cannot be distinguished on the plot. On the other hand, the reverse shock has already crossed almost 20 per cent of the mass of the ejecta. At $t = 5.2\times10^5$ s, i.e. $R \simeq 1.3\,R_{\rm dec}$, the reverse shock has almost finished to cross the ejecta, and the forward shock has just started to propagate: the shocked external medium has a mass of a few per cent of the initial mass of the ejecta, i.e. is of the order of M_0/Γ_0 (dark green line).

After $t \simeq 8\times10^5$ s, i.e. $R \simeq 2\,R_{\rm dec}$, the forward shock has accumulated a significant amount of external medium, and conversely, some of the initial ejecta has now left the simulation box on the left side (orange line). At $t = 9.17\times10^5$ s, 50 per cent of the initial mass of the ejecta has left the simulation domain (red line). The subsequent evolution is only driven by the forward shock and we recover the temporal evolution from analytic solution of Blandford & McKee (1976). However, as the shocked external medium accumulates more mass and becomes wider, it cannot be modeled properly within the size of our simulation box. After $t \simeq 1.8\times10^6$ s, i.e. $R \simeq 4.5\,R_{\rm dec}$, our simulation diverges from the Blandford & McKee (1976) and we discard its subsequent evolution.

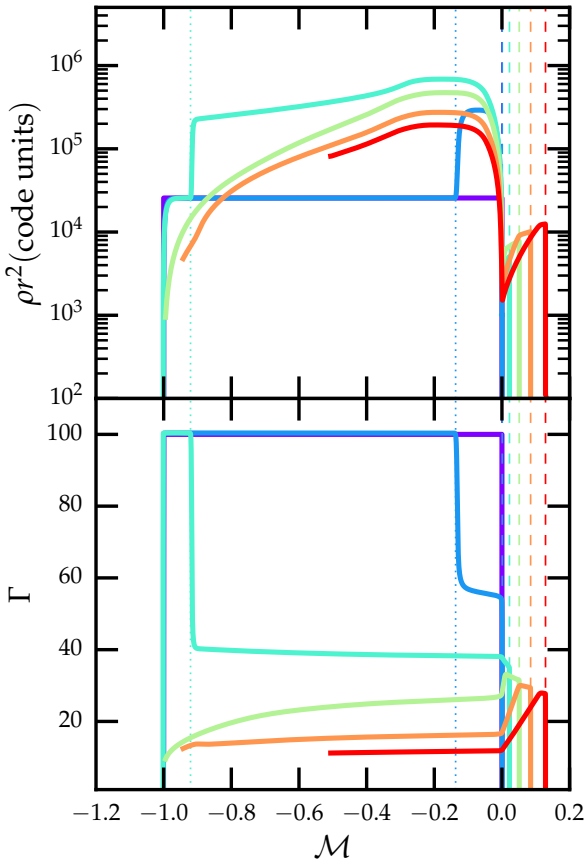

Figure 3. Hydrodynamics in *run1* with a uniform ejecta. Density (top) and Lorentz factor (bottom) as a function of the Lagrangian mass at $t = 0, 2\times10^5, 5.2\times10^5, 6.8\times10^5, 8.0\times10^5$ and 9.17×10^5 s (from purple to red). The contact discontinuity between the ejecta and the external medium is located at $\mathcal{M} = 0$ by definition. The forward and reverse shock are shown by dashed and dotted vertical lines respectively. We have multiplied the density by r^2 to remove the impact of spherical expansion and allow a better focus on shocked and expanding regions. After $t = 6.8\times10^5$ s the inner part of ejecta is out of the simulation domain.

3.2 Long-lived reverse shock

The luminosity of the afterglow may be altered if the reverse shock is long-lived. Therefore, we reduce the speed of the second half of the ejecta, with a linearly decreasing Lorentz factor in *run2*. Fig. 4 shows the evolution of *run2*, at the same times as *run1*. As the energy injection in both ejecta is set to be identical, the total mass in the ejecta in *run2* is about twice as large than in *run1*. The gradient in the Lorentz factor causes the ejecta to expand and form a tail of slow material, and a fraction of the ejecta is rapidly advected out of the simulation domain. As expected for this initial state, we observe a LLRS: (i) before the reverse shock reaches the tail of the ejecta around $t = 4\times10^5$ s (transition happens between blue and green lines), the evolution downstream of the reverse shock is exactly the same as for *run1*; (ii) afterwards, both runs evolve differently. Due to the slower and denser tail region, the propagation of the reverse shock is slowed down with respect to the uniform case and it leaves the simulation region at $t = 8.7\times10^5$ s (compared to 5.5×10^5 s in *run1*, transition happens between orange and red lines). Similarly, the slower tail region results in a slower forward shock.

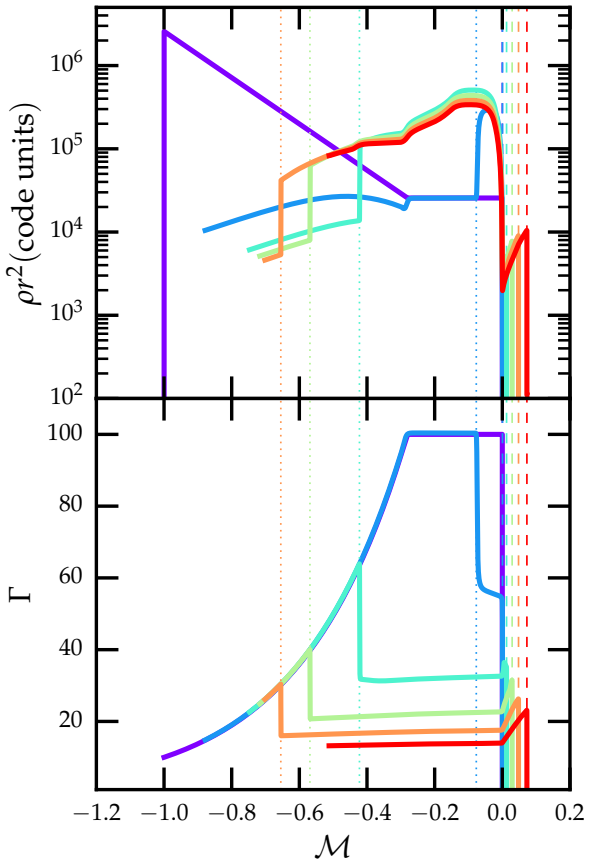

Figure 4. Hydrodynamics in *run2*, which includes a slower tail region. The timesteps and colors are the same as in Fig. 3.

3.3 Internal shocks

Internal shocks occur when the gradient of the Lorentz factor is strictly negative meaning faster material is behind slower material. We explore two different cases: when a head region is present ahead of the fastest part of the ejecta as in *run3* or when a sinusoidal variation in the Lorentz factor is present in the tail region as in *run4*. In both cases, we expect internal shocks to form and structure the ejecta, but the interaction of these shocks with the reverse shock should occur much earlier in *run3*. This is confirmed by the simulations.

Fig. 5 shows the evolution of *run3*, with the left panel focusing on the early development of an internal shock. We used Eulerian coordinates as they better highlight different discontinuities in the head region at this early stage. Initially, the Lorentz factor profile is very shallow, but it quickly steepens as faster material is behind slower material. We expect the formation of internal shocks at a radius $R_{\rm is} \simeq 2\,(k\Gamma_0)^2\,ct_{\rm var}$, where $t_{\rm var}$ is the variability timescale in the initial state, of the order of $0.5\,\beta t_{\rm w}$, i.e. $R_{\rm is} \simeq 4\,10^{14}$ cm. Indeed, we observe that after roughly 10^4 s, a denser shocked region has developed and two internal shocks appear (dot-dashed lines). However these shocks do not have time to propagate as, at $t = 1.5 \times 10^4$ s (transition happens between green and yellow lines), the reverse shock reaches the outer edge of the dense shocked region. This results in a reflected shock propagating forward, as can be seen at $t = 1.8 \times 10^4$ s (yellow line). This internal shock crosses the contact discontinuity at $t = 1.6 \times 10^4$ s (transition happens between yellow and orange lines) and eventually catches up with the forward shock in the external medium at $t = 2 \times 10^4$ s, reaccelerating it. The later propagation of the reverse shock is very similar to *run2*.

In *run4*, the negative Lorentz factor gradient is located in the tail region, where is has more time to develop into a dense shocked region before it becomes affected by the reverse shock at $t = 5 \times 10^5$ s. The left panel of Fig. 6 shows this initial development, until $t = 4.4 \times 10^5$ s. As the reverse shock interacts with the outermost internal shock, a shock reflection occurs and results in a forward propagating shock (see yellow line), similarly to *run3*. The latter will propagate into the shocked external medium (see red line) and eventually catch up with the forward shock. The propagation of the reverse shock lasts for almost 10^6 s, as it is significantly slowed down when crossing the dense region. When it eventually crosses the backward propagating internal shock, a reflected shock propagates forward again, which also eventually reaches the forward shock and slightly re-accelerates it (see red line). This evolution is in good agreement with the theoretical expectation described in section 4 of Hascoet et al. (2015). As described in Hascoet et al. (2015), this interaction of the reverse shock with the dense shell in the tail due to the formation of internal shocks will affect the luminosity and is a possible mechanism for observed flares in the afterglow.

3.4 Full evolution

Having identified the individual contributions of each feature, we analyze *run5*, which combines all previous features and provides a more complete insight on the evolution of a realistic GRB afterglow. The global evolution is essentially a combination between the impact of the early internal shocks present in *run3* and the later ones from *run4*. This setup leads to two internal shock regions, which both have a forward propagating shock and backwards propagating shock. The interaction between the latter and the reverse shock leads to reflected shocks, which propagate back to the forward shock.

Fig. 7 shows the Lorentz factor downstream each of these shocks over time, with the results of the ballistic model for the same initial state shown below. At $t = 7 \times 10^3$ s, the internal shocks in the head region become apparent (1) and persist until the reverse shock interacts with its forward propagating shock (2). This effectively damps the reverse shock, and the internal reverse shock is now considered as the reverse shock. A reflected shock is swiftly propagating forward until it catches up with the forward shock (4) and reaccelerates it significantly. In the meantime, a shocked region has formed in the tail region as well (3). As the reverse shock enters the tail region it is slowed down (5) until it is accelerated when encountering the internal shock region (6). Again, this interaction results in a forward propagating shock which is momentarily stalled at the contact discontinuity with the shocked external medium (7) and then catches up with the forward shock (10). The reverse shock eventually reaches the back shock of the internal shocked medium (8) and then leaves the simulation domain (9). In the next section we study the impact of the dynamics on the bolometric light curves of the ejecta.

Fig. 7 also highlights that in the ballistic model, the shocked regions behind the reverse shock and the forward shock have the same Lorentz factor, as behind the internal forward and reverse shocks. This is due to the lack of resolution in this approach, where shells merge after each collision. Generally, the Lorentz factors in the simulations bracket the value from the ballistic model. The Lorentz factor of the forward shock is usually underestimated

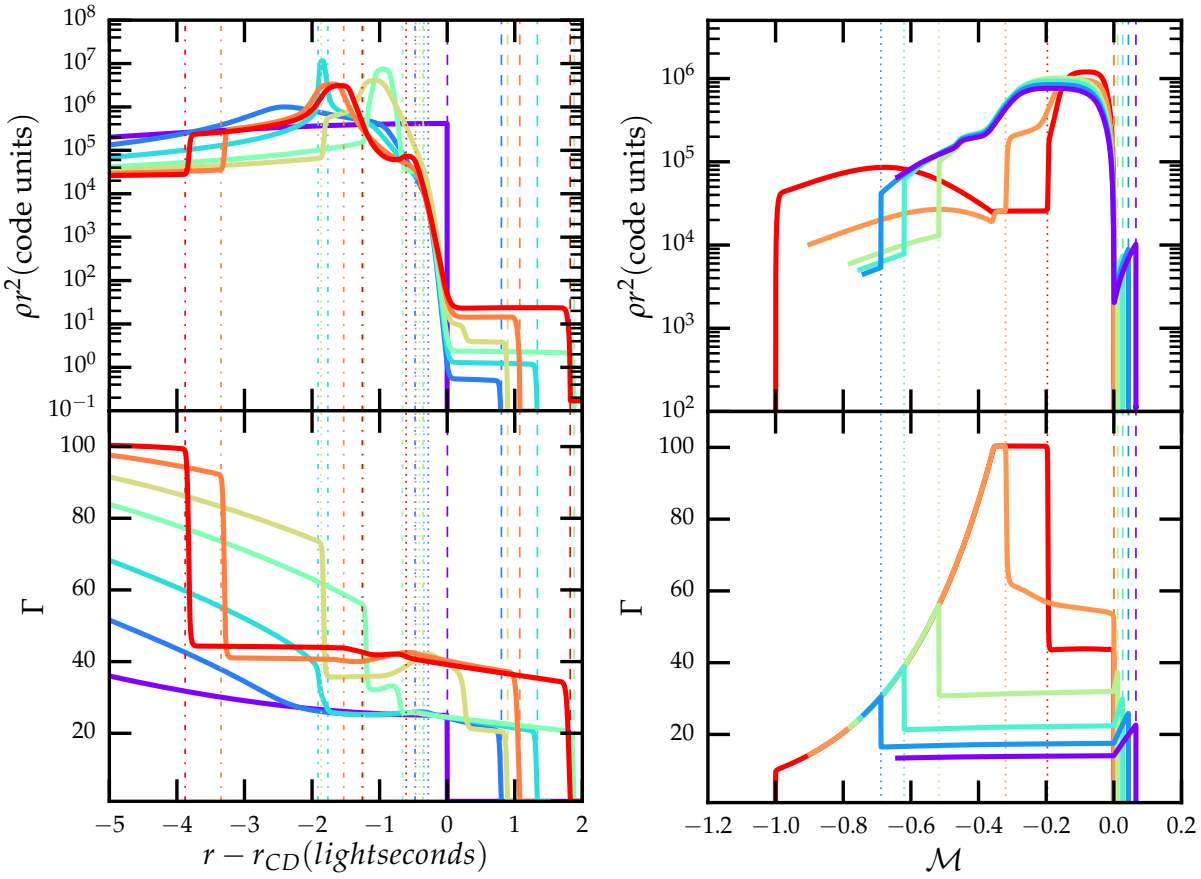

Figure 5. Hydrodynamics in *run3*, which includes a slower head region. Left: Eulerian view of the early evolution of the density and Lorentz factor at $t = 0, 6 \times 10^3, 1 \times 10^4, 1.4 \times 10^4, 1.8 \times 10^4, 2.7 \times 10^4$ and 3.6×10^4 s (from purple to red). The dotted, dot-dashed and dashed lines respectively show the position of the reverse, internal and forward shocks. Right: Lagrangian view of the later evolution, showing the same quantities at $t = 3.6 \times 10^4$ s, which is the latest timestep on the left panel (red), and $2 \times 10^5, 5.2 \times 10^5, 6.8 \times 10^5, 8.0 \times 10^5, 9.17 \times 10^5$ (from orange to purple). The timesteps on the right are the same as in Figs. 3,4.

while the reverse shock is modeled more accurately. Conversely, the downstream density in the ballistic model (not shown here) seems well reproduced for the forward shock, but strongly underestimated for the reverse shock. In the next sections we compare the resulting bolometric luminosity of both models.

4 EMISSION

4.1 Emission model

We compute the bolometric light curves for our different models and determine the contributions of the forward shock, internal shocks and reverse shock. At a given $t_{\rm obs}$ in the observer frame, the received bolometric luminosity from one shocked region is given by

$$L_{\rm bol}(t_{\rm obs}) = \int {\rm d}t 2\epsilon_e \frac{L_{\rm diss}(t)}{\Delta t_{\rm obs}(t)} \frac{1}{\left(1 + \frac{t_{\rm obs} - t_{\rm obs,0}(t)}{\Delta t_{\rm obs}(t)}\right)^3}, \quad (9)$$

where $\epsilon_{\rm e}$ is the fraction of the dissipated energy injected in non-thermal electrons, and where the integration over t (lab frame) is carried out during the time interval corresponding to the propagation of the considered shock. The dissipated energy in a given shock $L_{\rm diss}(t)$ is set by the variation of the internal energy between the downstream and upstream regions

$$L_{\rm diss}(t) = \dot{M}_s \Gamma_* (\epsilon_* - \epsilon) \quad (10)$$
$$= 4\pi r^2 \rho_* \Gamma_*^2 (V_s - v_*)(\epsilon_* - \epsilon), \quad (11)$$

where the subscript $*$ indicates quantities in a shocked region, $\dot{M}$ is the mass flow across the shock, ϵ the specific internal energy and V_s is the velocity of the shock, which is determined by comparing its position between outputs. $t_{\rm obs,0}(t)$ corresponds to the reception of the first photon in the observer's frame from on-axis emission at radius r and time t, i.e.

$$t_{\rm obs,0} = t - \frac{r}{c}, \quad (12)$$

while the timescale

$$\Delta t_{\rm obs}(t) = \frac{1}{h^2} \frac{r}{2\Gamma^2 c} \quad (13)$$

is the observed time delay between photons emitted at radius r and time t either on-axis or at an angle $1/(h\Gamma)$ corresponding to the beaming of half of the emission. We usually assume $h = 1$ (isotropic emission in the comoving frame). However, by adopting $h > 1$, we can also account for the possibility of anisotropic synchrotron emission in the comoving frame (Beloborodov et al. 2011).

As our main goal is to study the observable variability, we assume that electrons are fast-cooling, as expected in internal shocks,

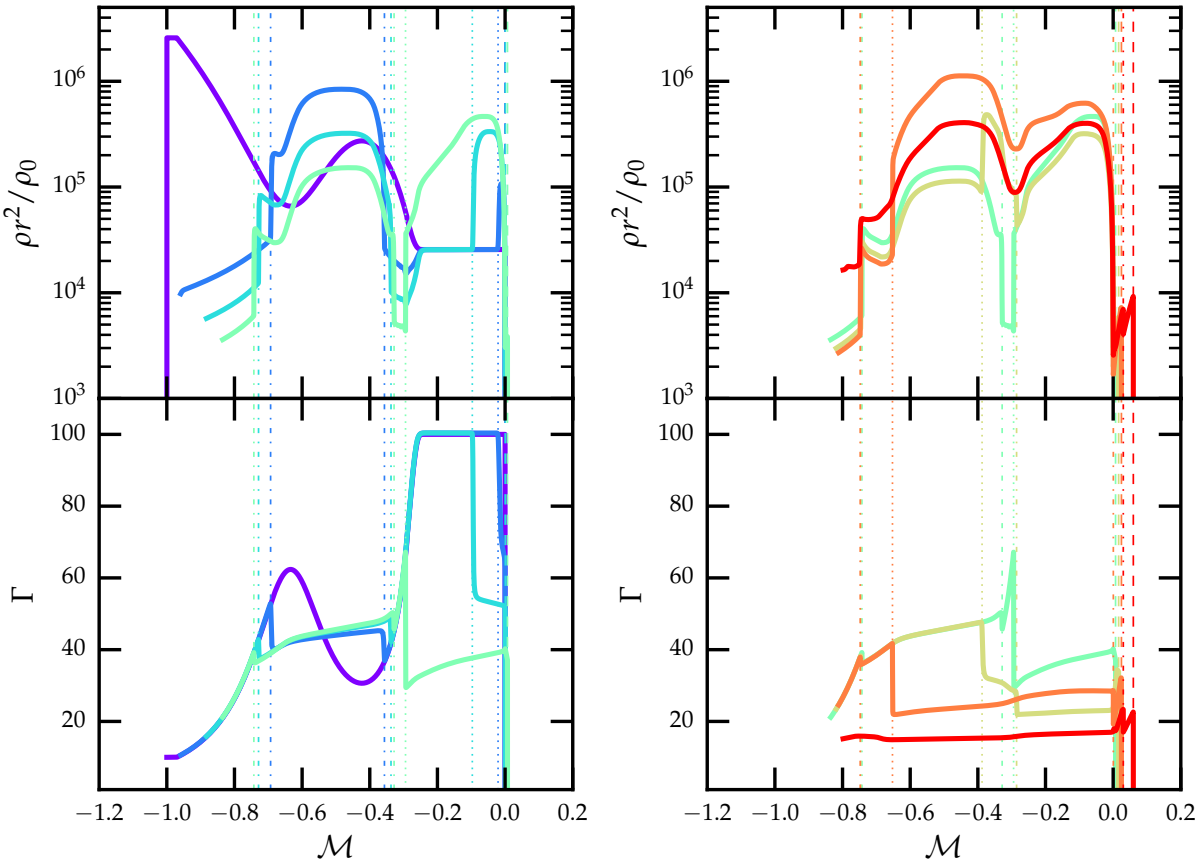

Figure 6. Hydrodynamics in *run4*, which includes variability in the tail region. Left: Early evolution showing $t = 0, 10^5, 2.3 \times 10^5$ and 4.4×10^5 s (from purple to green). Right : Later evolution showing $t = 4.4 \times 10^5, 5.7 \times 10^5, 6.5 \times 10^5$ and 8.7×10^5 s (from green to red).

or in collisions between the reverse shock and internal shocks. This is well adapted to study flares, but may not be necessarily true for the whole evolution of the underlying smooth component of the emission. In the following, we adopt $\epsilon_e = 1$ for all shocks, as it can be easily rescaled later.

In practice, for each output (corresponding to a given time t), we determine the location of the different shocks, and then for each of them determine $t_{\rm obs,0}$ and $\Delta t_{\rm obs}$ and the quantities in the shocked region to compute the corresponding $L_{\rm diss}$. To compute the bolometric light curve due to a given shock, for each t_{obs}, we add the contributions of all t using Eq. 9. We eventually add up the contributions of the different types of shocks.

4.2 Bolometric light curves

Fig. 8 shows the bolometric light curves for all runs and the result of the ballistic model. The left column shows only the contribution of the forward shock propagating in the external medium. In *run1*, its bolometric luminosity initially increases until the head of the ejecta starts decelerating at $t_{\rm obs} \simeq 200$ s, after what it follows the expected self-similar solution with a $t_{\rm obs}^{-1}$ slope (Blandford & McKee 1976). When the head of the ejecta is slower (*run3, run5*), the initial luminosity is naturally lower and suddenly rises after $t_{obs} = 20$ s when the forward shock is reaccelerated by the reflected forward shock (label '4' in Fig. 7). The forward shock is more luminous than for *run1* for a brief moment and the deceleration occurs earlier. Eventually, all runs converge to the same self-similar solution, consistent with the total amount of injected energy. The bump in *run4, run5* around $t_{\rm obs} \simeq 300$ s is caused by the reacceleration of the forward shock due to the internal forward propagating shock (the latter resulting from the reflection of the reverse shock on the internal shock region, label '10' in Fig. 7). The luminosity curves are in good agreement with the ballistic model shown below. In all cases, the simulations yield a slightly later deceleration of the ejecta.

The right column of Fig. 8 shows the sum of the contributions of all other shocks, which propagate within the relativistic ejecta. This includes the reverse shock, and the internal shocks in the tail and head regions, and represents the total internal dissipation. As suggested by the complex evolution of the Lorentz factor in Fig. 7, the bolometric light curves are not smooth and present a much higher variability than the lighturves from the forward shock. This important variability, which will be fully described in §5, confirms our initial motivation for this study.

For *run1*, the luminosity of the reverse shock progressively increases until it reaches the inner edge of the ejecta at $t = 5.2 \times 10^5$ s, corresponding to $t_{\rm obs} = 200$ s, after which only off-axis photons are received and the flux follows the expected $t_{\rm obs}^{-3}$ decrease. For *run2*, which includes a slower tail region and yields a LLRS, the decrease in luminosity starts earlier, when the reverse shock reaches the tail region. As the ejecta is more extended in this case, the reverse shocks remains active for a longer time and the luminosity ends up being larger than for *run1*. In both cases, the

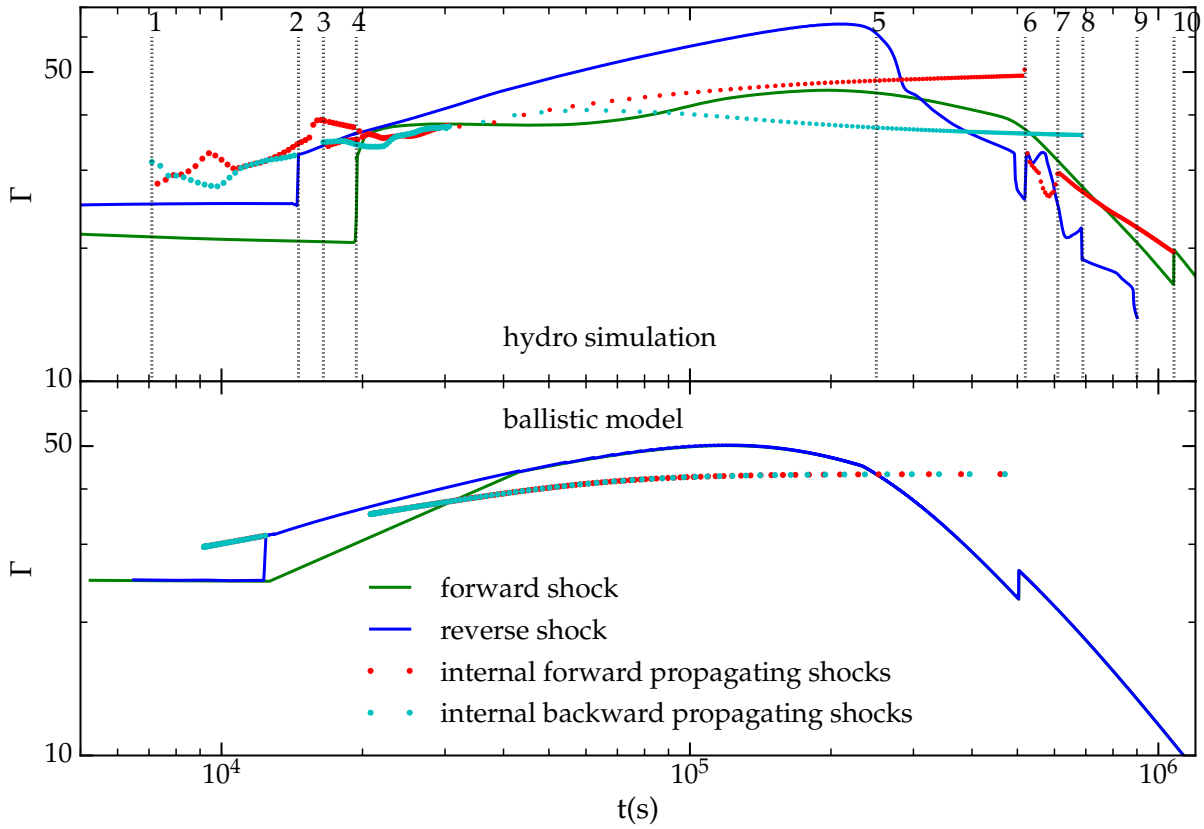

Figure 7. Lorentz factor in *run5*, which includes variability in the tail region and a slower head region. The upper and lower panels show the Lorentz factor in the shocked material behind the forward shock (FS), reverse shock (RS) and the internal forward (IFS) and backwards propagating shocks (IRS) in the hydrodynamic simulation and ballistic model respectively. Sudden variations are indicated with numbers and vertical lines and are detailed in the text.

ballistic model very well reproduces the simulation, with a slightly lower and steeper drop-off for the luminosity.

When the head region is present, as in *run3* and *run5*, the reverse shock is slower, and the emission very steeply rises around $t_{\rm obs} = 10-20$ s, when the reverse shock encounters the shocked region (label '2' in Fig. 7). The following decrease in flux is initially slow but recovers the same slope than *run2* after roughly 100 s. We do not recover the small upturn seen around $t_{\rm obs} = 70$ s in the ballistic model.

In *run3* and *run5*, the impact of the internal shocks in the head region is rapidly suppressed by the propagation of the reverse shock and this configuration is unlikely to produce important variability[1] On the other hand, internal shocks in the tail region produce a much stronger effect, as can be seen in *run4*. The initial evolution is identical to *run2* and the impact of the internal shock region becomes apparent around $t_{\rm obs} = 100$ s, just after the dimming of the reverse shock as it enters the tail region. As the reverse shock interacts with the internal shocked region, it gets revived and results in the reflected forward propagating shock. Both these effects account for the rebrightening at $t_{\rm obs} \simeq 250$ s, with the main contribution from the reflected shock. The ballistic model shows qualitatively similar results, although with lower emission at all times. In the following section we detail the observable properties of all the variability using our complete model from *run5*, and compare with the properties of the flares observed in the X-ray afterglow.

[1] However, variations of the Lorentz factor on shorter timescales would lead to earlier internal shocks, which could propagate without being smoothed out by the reverse shock. As our study does not focus on the prompt phase, we did not simulate such cases.

5 FLARES FROM A LLRS IN A STRUCTURED EJECTA

The first goal of this study is to establish the validity of the ballistic model used by Hascoet et al. (2015) to describe the dynamics of gamma-ray bursts ejecta and more specifically flares in the early afterglow phase. The bolometric light curves in Fig. 8 show a good qualitative agreement in all cases between the ballistic model and simulation. The light curves show similar slopes, timing for flares and relative luminosity between different configurations. However, we systematically find an increased luminosity in the hydrodynamic simulations for the reverse and internal shocks, and a slight delay for the deceleration of the forward shock. The increased luminosity may be due to the uncertainty in the definition of the upstream and downstream media. However, as we have detailed in §2.4, we are confident that our shock detection method yields the proper values soon after the beginning of the simulation. We have also tested that artificially increasing or decreasing $L_{\rm diss}$ and/or $\Delta t_{\rm obs}$ (see Eq. 10) at early times does not affect the luminosity at later times and cannot account for the discrepancy. As such, we expect that the difference between the ballistic model and our simulations reveals the weaknesses of the ballistic model. Specifically, the ballistic model underestimates the density in the shocked medium

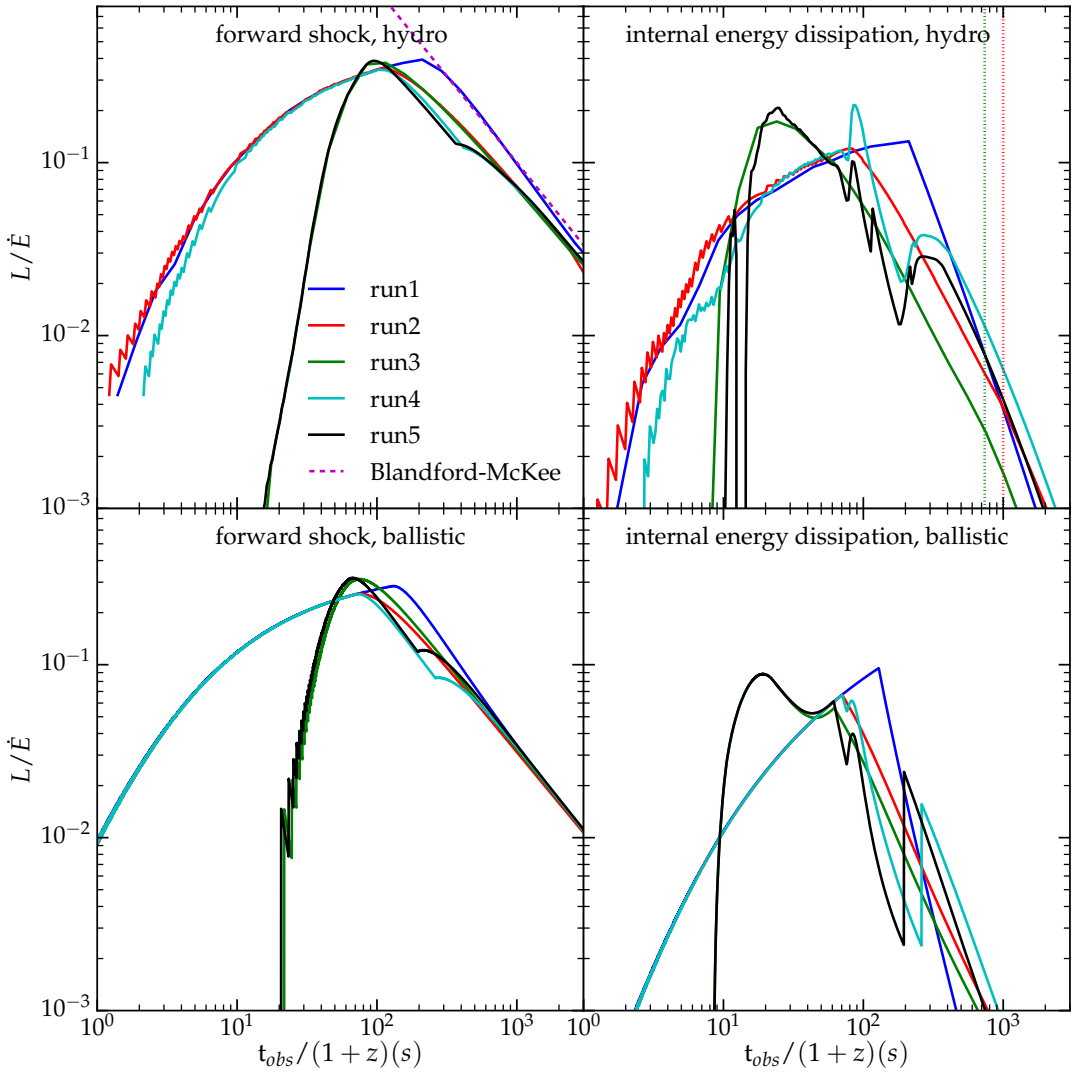

Figure 8. Bolometric light curves of the forward shock (left column) and internal and reverse shocks (right column) assuming isotropic emission in the comoving frame. The five main runs are shown (color coded), comparing the simulations (upper row) and the ballistic model (lower row). On the top-left panel, the magenta dashed line shows the $t_{\rm obs}^{-1}$ (Blandford & McKee 1976) self-similar solution. The dotted vertical lines indicate the time beyond which some of the off-axis emission is missing because the reverse shock has left the simulation domain. As seen in the right column, internal dissipation leads to flare-like features for $t_{obs} \geqslant 70$ s in *run4* and *run5*.

due to a poor spatial resolution intrinsic to the method, as already discussed in Daigne & Mochkovitch (2000).

In addition, shock reflections at late times, which strongly impact the late flare in *run4* and *run5* at $t_{\rm obs} \geqslant 70\,{\rm s}$ are missing in the ballistic model. Their impact was predicted by Hascoet et al. (2015) (see their §4) and is confirmed here.

Despite these discrepancies, the overall shapes of the curves and their respective order is the same in the model and the hydrodynamic simulations. This validates the determination of the forward shock in the ballistic model and our numerical setup with moving boundaries. The ballistic model is ideally suited to explore a wide range of parameters at negligible computational cost. However, the small quantitative differences may hinder the derivation of microphysical parameters based on direct comparison with observations.

In the set of simulations presented here, our assumptions on the initial structure of the ejecta are particularly important, as they lead to an internal structuration after the propagation of internal shocks, which will eventually produce flares in the light curve during the propagation of the LLRS. While we have considered highly idealized cases (see Fig. 2), negative gradients in the Lorentz factor are likely to arise naturally in the flow and a tail of slower material and can be expected from a fading central engine and/or the breakout of the ejecta through the stellar envelope in long bursts (see e.g. Duffell & MacFadyen 2015). More self-consistent modeling of the flow dynamics would require three dimensional simulations, which come at prohibitive cost for the study presented here.

Using these idealized simulations, we now discuss the variability expected in the afterglow light curve assuming that its X-ray emission is dominated by the contribution of internal dissipation in the ejecta, at least at early times. As discussed in Uhm & Beloborodov (2007); Genet et al. (2007); Uhm et al. (2012), this can happen if the forward shock is initially radiatively inefficient in the ultra-relativistic regime, due to an inefficient acceleration of electrons and/or an inefficient amplification of the magnetic field in the shocked external medium. With this assumption, we detail the properties of the flares produced by the propagation of a LLRS in a

structured ejecta, and compare them to observed flares in the X-ray afterglow. The cases with internal shock regions produce flare-like features in the light curve, due to the reverse and internal shocks contributions (both in the hydrodynamic simulations and with the ballistic model). The left panel of Fig. 9 shows the contribution to the light curve of all shocks but the external forward shock in *run5*. The ejecta produces four short flare-like features (shown with arrows), with peak luminosity at $t_{\rm obs} = 11, 84, 116, 214\,{\rm s}$ and a longer bright flare around $t_{\rm obs} \simeq 300\,{\rm s}$ (shown with a shaded grey region).

The first short flares, indicated by arrows in Fig 9, have $\Delta t_{\rm obs}/t_{\rm obs} \simeq 0.2$, and are solely caused by the emission from internal shocks. As such, they are directly related to the initial stratification of the ejecta due to variability in the central engine, which has already be described in previous studies (Rees & Meszaros 1994; Kobayashi et al. 1997; Daigne & Mochkovitch 1998, 2000). Our results illustrate that late internal shocks can produce early flares in the afterglow, especially during the early steep decay phase. However, the same mechanism would require a long-lasting central engine to also produce late flares (Burrows et al. 2005b; Fan & Wei 2005; Zhang et al. 2006).

The last, bright, and longer flare, appears at $t_{\rm obs} \sim 300\,{\rm s}$, much after the initial ejection with t_w=100 s. It has a more complex origin, as it is a combination of emission due to the reverse shock (solid red line) and the forward propagating internal shock (dashed red line). In the ballistic model, this second component is missing. The increased emission from the reverse shock starts at $t_{\rm obs} = 181\,{\rm s}$, when it enters the overdense internal region (label '6' in Fig. 7) and drops steeply after $t_{\rm obs} = 335\,{\rm s}$, when it exits the shocked region (label '8' in Fig. 7). The interaction of the reverse shock with the shocked region causes the reflection and rebrightening of the forward internal shock towards the front of the ejecta. The emission from the internal forward shock abruptly drops at $t_{\rm obs} = 350\,{\rm s}$, when it has reached the forward shock (label '10' in Fig. 7). The long duration of the rebrightening, and the plateau-like emission between $250 - 400\,{\rm s}$ is due to the combined emission of both shocks. As such, it leads to a bright feature in the light curve, but with properties which seem in contradiction with observations of X-ray flares: the flare is too broad and flat. We discuss below several effects that may solve this problem.

- *Impact of the external density.* In the right panel of Fig. 9, we show light curves from *run5b*, which is identical to *run5* except that the external density is set to $n_0 = 32\,{\rm cm}^{-3}$. The lower density leads to a delayed deceleration of the ejecta and a lower density for the shocked external medium, resulting in a later development of the reverse shock. In this case, the emission from the internal forward shock is much lower than in *run5* and the emission after $t_{\rm obs} \simeq 400\,{\rm s}$ is dominated by the reverse shock and is much more flare-like. We infer that the plateau-like emission in *run5* is the result from a peculiar choice of initial conditions, which made the emission of the reverse shock and internal forward shock of comparable magnitude and slightly shifted in time. In other configurations, the emission from the LLRS is much more temporally separated and flare-like. Again, we note that in *run5b*, the last bright flare due to the LLRS appears at $t_{\rm obs} \sim 500$ s which is much after the end of the ejection($t_w = 100$ s). This illustrates the capacity of this scenario to produce late flares without invoking a long-lasting central engine.
- *Spectral range of the emission.* When the flare-like features are produced by a single shock, it is legitimate to assume that the X-ray light curve has the same shape as the bolometric one if electrons radiating in X-rays are fast-cooling. In the last flare observed in *run5*, the situation is more complex, with contributions of two different shocks (IFS and LLRS). We now consider the possibility that the synchrotron emission from accelerated electrons in the two shocked regions occur at different frequencies.

  Assuming that the energy injected in the magnetic field (ϵ_B) and in non-thermal electrons (ϵ_e) is the same in the internal and reverse shocks, the frequency of the synchrotron emission varies as $\nu_s \propto \Gamma_* \epsilon_*^{5/2} \rho_*^{1/2}$. Fig. 10 shows the specific internal energy ϵ_* at the reverse shock and internal forward shock for *run5*. The values of the density and Lorentz factor are similar in both shocked regions (see §3). As the ratio of ϵ_* between the IFS and the RS is $\simeq 30$ around $t_{obs} \simeq 220$ s, this suggests that the emission of the internal forward shock has a much higher frequency during the last flare. Depending on microphysics parameters, this can lead to two possibilities: (i) either the X-ray light curve is dominated by the RS, leading then to a late flare with a shape and a duration which look much like those of observed X-ray flares. In this case, one could expect a short precursor in gamma-rays due to the IFS; (ii) or the X-ray light curve is dominated by the IFS, leading to a narrow flare followed by a longer ones at lower frequency. Clearly, this could be a source of chromatic variability in the afterglow. To test these possibility, one needs to implement the calculation of the synchrotron emission from all shocks, which we leave to a further study.

Still, in the most favorable cases showing a later flare with a fast rise and a slower decay around, i.e. *run5b* or *run5* assuming that the IFS does not significantly contribute in X-rays, the width of the last flare $\Delta t_{\rm obs}/t_{\rm obs} \simeq 1$ is larger than in observed X-ray flares ($\Delta t_{\rm obs}/t_{\rm obs} \simeq 0.1 - 0.3$, Chincarini et al. 2007). A possible solution is an anisotropic synchrotron emission in the comoving frame, as suggested by Beloborodov et al. (2011). This results in $h > 1$ in Eq. 13. Fig. 11 shows the light curves for *run5* and *run5b* in the standard (isotropic) case and in the case where 75% of the emission is beamed within $\theta = 60^\circ$ in the comoving frame, i.e. $h^2 = 3$. The latter shows more temporally peaked emission, with a higher peak luminosity resulting from limb darkening, in a much better agreement with observations (Chincarini et al. 2007).

Our study confirms the predictions by Hascoet et al. (2015) with a much more detailed description of the dynamics: assuming moderate anistropy of the emission in the comoving frame, and an radiatively less efficient external forward shock, the propagation of a LLRS in a stratified relativistic ejecta produces flares in the afterglow, with properties comparable to those of observed X-ray flares. The stratification is naturally obtained at the end of the internal shock phases, which lead to the formation of dense shells with uniform Lorentz factor in the ejecta.

6 CONCLUSION

In this paper, we present a set of high resolution one-dimensional relativistic hydrodynamic simulations of a stratified GRB ejecta interacting with a uniform external medium in order to study the variability of the early afterglow. We follow the power dissipated in each shocked region (external foward shock, internal shocks, reverse shock) and compute the resulting bolometric light curves, assuming synchrotron radiation of shock accelerated electrons in the fast-cooling regime.

The resulting bolometric light curves agree well with a ballistic model (Daigne & Mochkovitch 1998; Hascoet et al. 2015). In particular, the ballistic model is able to reproduce the slopes and

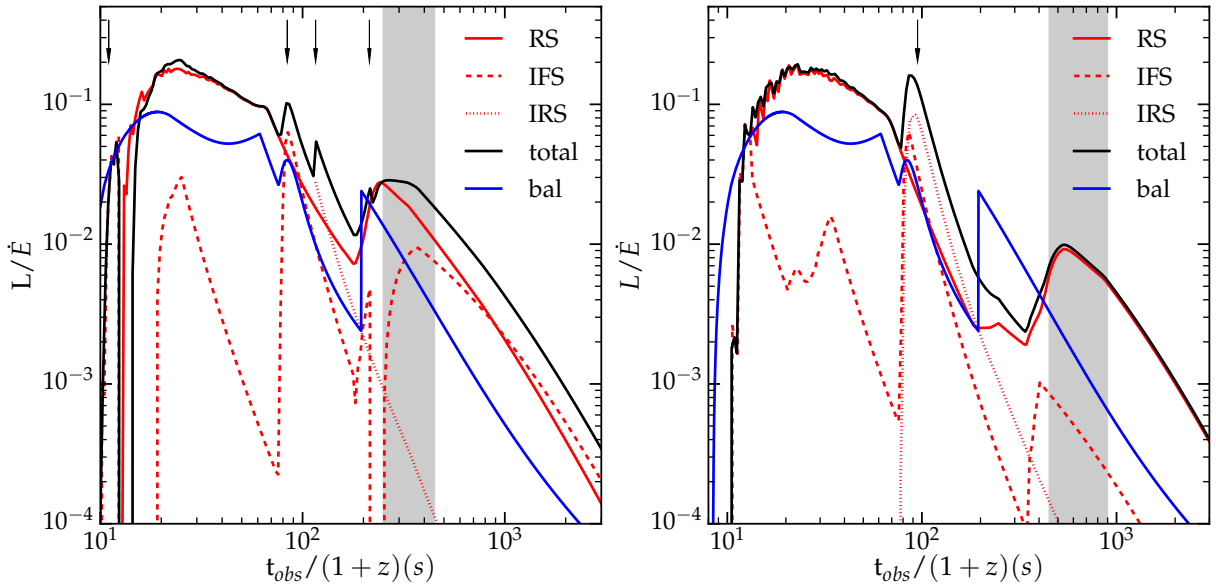

Figure 9. Separate contributions to the light curve in *run5* (left) and *run5b* with a lower external density (right). The total contributions of all shocks but the external forward shock is shown in black, and compares well with the ballistic model (blue). The arrows and shaded region respectively indicate short and long-duration flares.

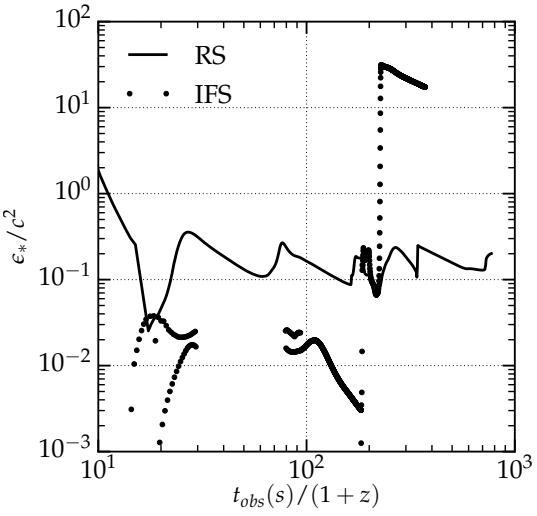

Figure 10. Internal energy in the internal forward shock (IFS) and reverse shock (RS) in *run5*.

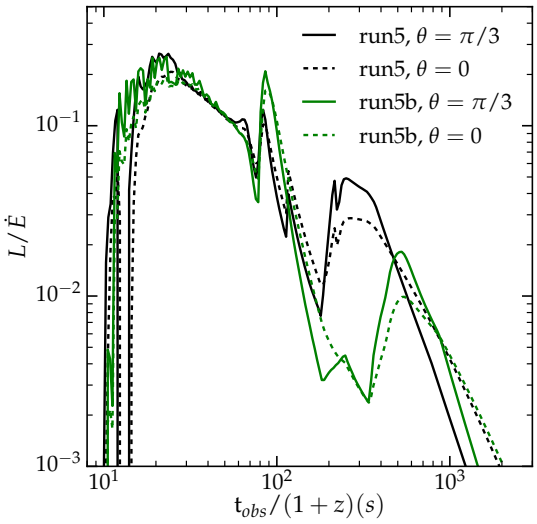

Figure 11. Light curves resulting from internal energy dissipation with isotropic ($\theta = 0$) and anisotropic emission for *run5* and *run5*. The emission from the forward shock is not included in these light curves. During the last bright flare, it is dominated by the LLRS, with a contribution of the IFS in *run5* (see Fig. 9).

relative variations of the light curves, albeit with a slightly lower total emission. However, our simulations provide a more accurate description of the dynamics: the ballistic model underestimates the density in the shocked medium, as already pointed out by Daigne & Mochkovitch (2000), and neglects shock reflections at late times. This validates its use for preliminary studies, as its low computing time allows for the exploration of a large range of parameters, but points out its limitation, that can impact the determination of microphysics parameters when comparing the model with observations.

We have used these simulations to validate the scenario proposed by Hascoet et al. (2015) for the origin of X-ray flares in GRB afterglows. Our results confirm that the propagation of a long-lived reverse shock in a stratified relativistic ejecta leads to the appearance of bright flares in the bolometric light curve of the internal dissipation (i.e. all shocks except for the external forward shock). Indeed, dense shells are formed after the propagation of internal shocks , which can produce early short flares in the afterglow. Later flares appear when the reverse shock interact with these shells. Compared to the approach used by Hascoet et al. (2015), our simulations allow to accurately model this interaction, which includes shock reflections that were predicted but could not be captured by the ballistic model. More specifically, the simulations show that:

(i) Late internal shocks can be a source of early variability in the afterglow.

(ii) The interaction of the long-lived reverse shock with a dense

shell in the ejecta yield a strong flare-like rebrightening, with a fast rise and slower decay.

(iii) Assuming the synchrotron emission is anisotropic in the comoving frame, the width of this flare is of the order of $\Delta t_{\rm obs}/t_{\rm obs} \sim 0.1 - 0.3$, in agreement with the properties of observed X-ray flares.

(iv) The time at which the flare is observed depends only on the initial properties of the ejecta (distribution of the Lorentz factor, kinetic energy) and on the external density. Flares can be observed at late time, without any need for a long-lasting central engine.

(v) The shocked regions behind the internal shocks and the long-lived reverse shock can have a very different internal energy. In such case, we expect the two shocks to contribute in different spectral ranges, which can lead to an interesting chromatic variability.

For this promising scenario to work, there is no constraint on the lifetime of the central engine as long as it is comparable to the GRB duration. On the other hand, several other assumptions are necessary:

- The GRB ejecta must be initially variable, to allow for the formation of internal shocks and the stratification of the ejecta with dense shells.
- A long-lived reverse shock must form. This is naturally expected if the central engine switches off smoothly, ejecting a tail of low-Lorentz factor material behind at the end of the relativistic ejecta.
- Synchrotron emission in the fast electron cooling regime is the dominant emission mechanism in X-rays when the long-lived reverse shock encounters the dense shells. This will be tested in a further study including the calculation of the synchrotron radiation.
- The emission of this long-lived reverse shock must dominate over the emission of the external forward shock, at least at early times when the X-rays are emitted. This is probably the strongest assumption but is possible if electron acceleration and/or magnetic field amplification is inefficient in the shocked external medium, behind the ultrarelativistic forward shock. As mentioned in Hascoet et al. (2015), this condition can be achieved at least during flares, as the shocked region behind the reverse shock suddenly becomes much denser and hotter.

Additional simulations are needed to explore a larger range of parameters, both for the ejecta and the external medium (such as wind-like configurations). This would allow to confirm that a large range of arrival times can be obtained for flares, as is found using the ballistic model. However, the set of simulations presented in this paper already illustrates the capacity of the long-lived reverse shock model to explain the observed diversity and variability of GRB early afterglows.

ACKNOWLEDGMENTS

The authors thank Zakaria Meliani for helpful advice on the setup of the simulations and Robert Mochkovitch for his insight on this manuscript. The authors thank the French Programme National Hautes Energies (PNHE) and the Centre National d'Etudes Spatiales (CNES) for financial support. Support for A. Lamberts was provided by an Alfred P. Sloan Research Fellowship, NASA ATP Grant NNX14AH35G, and NSF Collaborative Research Grant 1411920 and CAREER grant 1455342. Numerical simulations were run on supercomputer Pleiades from the NASA Supercomputing Division and supercomputer Stampede from the Texas Advanced Supercomputing Center.

REFERENCES

Aloy M. A., Ibáñez J. M., Martí J. M., Gómez J.-L., Müller E., 1999, ApJ, 523, L125
Aloy M. A., Müller E., Ibáñez J. M., Martí J. M., MacFadyen A., 2000, ApJ, 531, L119
Beloborodov A. M., Daigne F., Mochkovitch R., Uhm Z. L., 2011, MNRAS, 410, 2422
Beniamini P., Kumar P., 2016, MNRAS, 457, L108
Berger E., 2014, ARA&A, 52, 43
Blandford R. D., McKee C. F., 1976, Physics of Fluids, 19, 1130
Burrows D. N., et al., 2005a, Space Sci. Rev., 120, 165
Burrows D. N., et al., 2005b, Science, 309, 1833
Chincarini G., et al., 2007, ApJ, 671, 1903
Chincarini G., et al., 2010, MNRAS, 406, 2113
Corrales L. R., Haiman Z., MacFadyen A., 2010, MNRAS, 404, 947
Dai Z. G., Lu T., 2002, ApJ, 565, L87
Daigne F., Mochkovitch R., 1998, MNRAS, 296, 275
Daigne F., Mochkovitch R., 2000, A&A, 358, 1157
De Colle F., Granot J., López-Cámara D., Ramirez-Ruiz E., 2012, ApJ, 746, 122
Duffell P. C., MacFadyen A. I., 2013, ApJ, 775, 87
Duffell P. C., MacFadyen A. I., 2015, ApJ, 806, 205
Fan Y. Z., Wei D. M., 2005, MNRAS, 364, L42
Gat I., van Eerten H., MacFadyen A., 2013, ApJ, 773, 2
Gehrels N., et al., 2004, ApJ, 611, 1005
Genet F., Daigne F., Mochkovitch R., 2007, MNRAS, 381, 732
Granot J., Piran T., Bromberg O., Racusin J. L., Daigne F., 2015, Space Sci. Rev., 191, 471
Hascoët R., Uhm Z. L., Mochkovitch R., Daigne F., 2011, A&A, 534, A104
Hascoët R., Daigne F., Mochkovitch R., 2012, A&A, 541, A88
Hascoët R., Daigne F., Mochkovitch R., 2014, MNRAS, 442, 20
Hascoet R., Beloborodov A. M., Daigne F., Mochkovitch R., 2015, preprint, (arXiv:1503.08333)
Kobayashi S., Piran T., Sari R., 1997, ApJ, 490, 92
Kobayashi S., Piran T., Sari R., 1999, ApJ, 513, 669
Kumar P., Zhang B., 2015, Phys. Rep., 561, 1
Lamberts A., Fromang S., Dubus G., Teyssier R., 2013, A&A, 560, A79
Margutti R., Bernardini G., Barniol Duran R., Guidorzi C., Shen R. F., Chincarini G., 2011, MNRAS, 410, 1064
Medvedev M. V., Loeb A., 1999, ApJ, 526, 697
Meliani Z., Keppens R., Casse F., Giannios D., 2007, MNRAS, 376, 1189
Mészáros P., Rees M. J., 1997, ApJ, 476, 232
Mimica P., Giannios D., Aloy M. A., 2009, A&A, 494, 879
Narayan R., Kumar P., Tchekhovskoy A., 2011, MNRAS, 416, 2193
Nousek J. A., et al., 2006, ApJ, 642, 389
O'Brien P. T., et al., 2006, ApJ, 647, 1213
Ramirez-Ruiz E., García-Segura G., Salmonson J. D., Pérez-Rendón B., 2005, ApJ, 631, 435
Rees M. J., Meszaros P., 1994, ApJ, 430, L93
Rees M. J., Mészáros P., 1998, ApJ, 496, L1
Rezzolla L., Zanotti O., 2002, Physical Review Letters, 89, 114501
Rezzolla L., Zanotti O., Pons J. A., 2003, Journal of Fluid Mechanics, 479, 199
Rowlinson A., O'Brien P. T., Metzger B. D., Tanvir N. R., Levan A. J., 2013, MNRAS, 430, 1061
Sari R., Mészáros P., 2000, ApJ, 535, L33
Sari R., Piran T., 1995, ApJ, 455, L143
Sari R., Piran T., Narayan R., 1998, ApJ, 497, L17
Sedov L., 1969, Similarity and dimensional methods in mechanics. Academic Press Inc.
Tagliaferri G., et al., 2005, Nature, 436, 985
Teyssier R., 2002, A&A, 385, 337
Troja E., et al., 2007, ApJ, 665, 599
Uhm Z. L., Beloborodov A. M., 2007, ApJ, 665, L93
Uhm Z. L., Zhang B., Hascoët R., Daigne F., Mochkovitch R., Park I. H., 2012, ApJ, 761, 147
Woosley S. E., 1993, ApJ, 405, 273

Zanotti O., Rezzolla L., Del Zanna L., Palenzuela C., 2010, A&A, 523, A8
Zhang B., Fan Y. Z., Dyks J., Kobayashi S., Mészáros P., Burrows D. N., Nousek J. A., Gehrels N., 2006, ApJ, 642, 354
Zhang B., Lü H.-J., Liang E.-W., 2016, Space Sci. Rev., 202, 3
van Eerten H., Zhang W., MacFadyen A., 2010, ApJ, 722, 235